Achieving a high-strength dissimilar joint of T91 heat-resistant steel to 316L stainless steel via friction stir welding

Zhiwei Wang[1,3,4], *Min Zhang*[1,3,4], *Cong Li*[2], *Fenglei Niu*[2], *Hao Zhang*[1,3], *Peng Xue*[1,3],✉, *Dingrui Ni*[3],✉, *Bolv Xiao*[3], *and Zongyi Ma*[1,3]

1) CAS Key Laboratory of Nuclear Materials and Safety Assessment, Institute of Metal Research, Chinese Academy of Sciences, Shenyang 110016, China
2) School of Nuclear Science and Engineering, North China Electric Power University, Beijing 102206, China
3) Shi Changxu Innovation Center for Advanced Materials, Institute of Metal Research, Chinese Academy of Sciences, Shenyang 110016, China
4) School of Materials Science and Engineering, University of Science and Technology of China, Shenyang 110016, China

Abstract: The reliable welding of T91 heat-resistant steel to 316L stainless steel is a considerable issue for ensuring the safety in service of ultra-supercritical power generation unit and nuclear fusion reactor, but the high-quality dissimilar joint of these two steels was difficult to be obtained by traditional fusion welding methods. Here we improved the structure–property synergy in a dissimilar joint of T91 steel to 316L steel via friction stir welding. A defect-free joint with a large bonding interface was produced using a small-sized tool under a relatively high welding speed. The bonding interface was involved in a mixing zone with both mechanical mixing and metallurgical bonding. No obvious material softening was detected in the joint except a negligible hardness decline of only HV ~10 in the heat-affected zone of the T91 steel side due to the formation of ferrite phase. The welded joint exhibited an excellent ultimate tensile strength as high as that of the 316L parent metal and a greatly enhanced yield strength on account of the dependable bonding and material renovation in the weld zone. This work recommends a promising technique for producing high-strength weldments of dissimilar nuclear steels.

Keywords: heat-resistant steel; stainless steel; friction stir welding; dissimilar welding; microstructure; mechanical property

1. Introduction

Ultra-supercritical (USC) power generation units and nuclear fusion reactors are crucial facilities to produce electric energy under the current severe situation of energy shortage. The development of the above equipment can not only improve the power generation efficiency but also reduce fuel consumption and damaging gas emissions [1–2]. Structural materials with superior thermostability should be used during the construction of these facilities due to the harsh service environment of high temperature, high pressure, and radiation medium [3]. T91 martensitic heat-resistant steel and 316L austenitic stainless steel are two promising candidate materials for assembling components of the USC unit and the nuclear fusion reactor due to their excellent corrosion and creep resistance to high-temperature steam [4–8]. For instance, the T91 steel is commonly used for fabricating the cooling pipes, and 316L stainless steel is widely used for vacuum vessels or valves. Therefore, it is inevitable to produce dissimilar joint between the T91 steel and 316L steel.

Welding is an efficient and reliable route that is frequently used in joining similar or dissimilar materials. Over the years, dissimilar joints of Cr–Mo (the main alloying component of

T91 steel) steels or Cr–W steel to 316L steel have attracted many investigations on their microstructures and mechanical properties. Defect-free joints have been obtained using traditional fusion welding methods, such as gas tungsten arc welding (GTAW) [9–10], electron beam welding [11–14], or fiber laser welding [13,15–16]. However, serious coarsening of microstructures was commonly detected in the weld metal due to the remelting and solidification caused by the large welding heat input [9–10,12,16].

At the T91 side, hard yet brittle lath martensite (M) with a high density of dislocations promoted the susceptibility to cold-cracking induced failure, and thus affected the safety of weldment in the course of service. In addition, the dissolution of the $M_{23}C_6$ phase in the heat-affected zone (HAZ) was a critical issue for fusion welding, which could deteriorate the high-temperature properties such as creep resistance of heat-resistant steels [10]. Hence, a post-weld heat treatment that prolonged the assembling period was frequently adopted to relieve the residual stress and enhance the joint's properties [9,13,17], which was very inconvenient for industrial application. At the 316L side, Cr enriched delta ferrite (F) which could reduce the corrosion resistance was generated in the HAZ at elevated temperature [10,18]. Consequently, a new

---

Ⓩ Springer

welding process with low heat input was required for joining T91 steel to 316L steel.

Friction stir welding (FSW), a solid-state welding process with depressed heat effect and significant grain refinement [19], was proposed to joint aluminum alloys [20], magnesium alloys [21], and polymers [22] which were hard to be welded by traditional fusion methods. In recent years, FSW has exhibited the potential of welding steels due to its feasibility in tailoring the microstructures and mechanical properties of joints [23–24]. Hence, it is viable to resolve the welding problems and improve the welding quality of dissimilar steel joints by using FSW. Recently, He *et al.* [25–26] and Tang *et al.* [27] verified the practicality of FSW to fabricate defect-free joints of 9Cr–1W steel to 316L stainless steel. Apparent grain refinement was achieved in the stir zone (SZ). However, obvious HAZ softening was detected at the 9Cr–1W steel side due to the coarsening and aggregation of precipitates, which implied a weak area where the failure occurred as the loss of creep strength. Sunilkumar *et al.* [18] obtained dissimilar joints of P9 steel (similar to T91 steel) to 316L stainless steel. They declared that higher strength could be achieved in FSW joint compared to GTAW joint. Nevertheless, the joint forming, especially the rough bottom surface and deficient in material mixing should be ameliorated to eliminate the potential creep failure locations.

This work aims to improve the forming quality as well as modify the HAZ heterogeneity of dissimilar FSW joints of T91 steel to 316L steel by designing the tool size and welding parameters. The microstructural evolution across the joint and near the bonding interface was carefully observed based on achieving defect-free joints by assessing the macromorphology. By comprehending the mechanical properties such as tensile and failure behaviors, the structure–property relationship of the FSW joint was well discussed.

2. Experimental

### 2.1. Materials and welding configuration

2 mm-thick T91 heat-resistant steel and 316L stainless steel sheets were used as the parent materials (PMs) whose chemical components were presented in Table 1. Before welding, the T91 steel sheets were normalized at 1050°C for 10 min followed by water quenching to ambient temperature and then tempered at 750°C for 1 h. The 316L steel sheets suffered solution heat treatment of 1060°C for 4 h. The above two types of steel sheets with a dimension of 60 mm × 15 mm were butt welded using a displacement-controlled FSW machine. As shown in Fig. 1(a), W–25Re alloy was used to make a small-sized tool with 5 mm in shoulder radius, 2 mm in pin radius, and 1.7 mm in pin length. During the welding process, the tool rotated and moved along the butt surface with a tilt angle of 3° relative to the normal direction. The tool rotation rates of 300–500 r/min were adopted with a consistent welding speed of 150 mm/min which was relatively higher than that used in the reported studies [18,25–26,28]. During FSW process, it is acknowledged that higher peak temperature and stronger plastic deformation are commonly achieved at the advancing side (AS) than the retreating side (RS) [29]. Based on this recognition, T91 steel was placed at the AS and 316L steel at the RS in view of minimizing the welding defect induced by a lack of deformation in T91 steel which possessed higher strength and hardness than 316L steel.

Table 1.   Chemical composition of T91 and 316L steels   wt%

Material	Cr	Ni	Mo	Mn	Si	C	S	P	Fe
T91	9.24	0.16	0.96	0.47	0.28	0.089	0.006	0.021	Bal.
316L	16.31	10.15	2.04	1.85	0.92	0.028	0.026	0.023	Bal.

2.2. Microstructural characterization

The cross-sectional microstructures of the joint were ob-
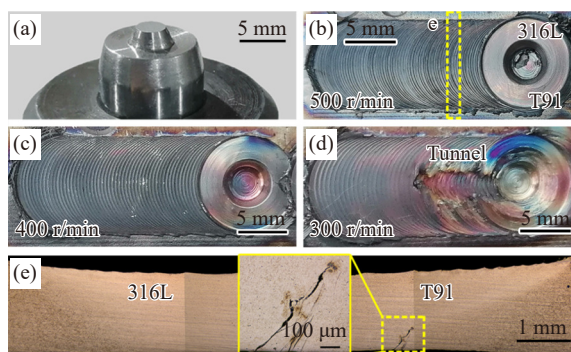
Fig. 1.   Macromorphologies of stir tool and as-welded joints: (a) stir tool used in this work, (b–d) top surface images of joints under various rotation rates, and (e) cross-sectional observation of 500 r/min joint.

served by a Leica DMi8M optical microscope (OM). The phase composition and grain structure were carefully examined using a Zeiss Supra 35 scanning electron microscope (SEM) which was equipped with an electron backscatter diffraction (EBSD) module. The characteristics of precipitates and bonding interface were detected by a ThermoFisher Talos F200X transmission electron microscope (TEM). The OM, SEM, and EBSD specimens were cut from the as-welded joint perpendicular to the welding direction. The specimens were ground, polished, and etched with appropriate solutions for OM and SEM observation. The T91 steel was etched with 10 g $CuSO_4$ + 50 mL HCl + 50 mL H_2O solution, while the 316L steel was revealed by electrolytic etching in a 10vol% oxalic acid + 90vol% H_2O solution at 5 V for 15 s. Before the EBSD examination, vibration polishing was applied to the mechanically polished specimen for removing the surface stress. TEM foils were cut across the bonding interface using the focused ion beam (FIB) technique. The chem-

168

Int. J. Miner. Metall. Mater., Vol. 30, No. 1, Jan. 2023

ical component evolution adjacent to the bonding interface was investigated by energy dispersive spectrometer (EDS) in both the SEM and TEM.

2.3. Mechanical assessment

Hardness examination was conducted on the polished OM sample surface along the normal direction (weld center) and transverse direction (thickness center) by using a LECO LM 247AT Vickers microhardness tester. An applied load of 1.96 N and a dwell time of 15 s were applied to each of the testing sites with a distance between the adjacent points of 0.1 or 0.2 mm. Tensile specimens of the joint were cut along the transverse direction with a gauge size of 20 mm length and 2.5 mm width. The tensile procedures were operated in an Instron 8801 testing system with an initial strain rate of 1×10^{-3} s^{-1} at room temperature. Meanwhile, a mechanical extensometer with a span length of 12.5 mm was used to measure the actual strain of the tensile specimens.

3. Results and discussion

3.1. Macromorphology

Fig. 1(b)–(d) shows the top surface morphologies of dissimilar FSW joints. Under a high rotation rate of 500 r/min, no macroscopical forming defect was found by observing both the top and bottom surfaces. However, a crack about 0.6 mm in length was found at the T91 side after dissecting the joint via a cross-sectional OM specimen (Fig. 1(e)). The sampling location was marked by yellow dotted lines as shown in Fig. 1(b). When decreasing the rotation rate to 400 r/min, a sound joint without any visible defect was successfully fabricated (Fig. 1(c)). In order to explore a lower heat input condition, the rotation rate was further decreased to 300 r/min. However, an apparent tunnel defect was formed around the stir pin on account of insufficient plastic material flow (Fig. 1(d)). Hence, 400 r/min was the optimum welding parameter which was analyzed detailedly in the following. Note that no obvious tool wear or deformation was found under different welding parameters.

As shown in Fig. 2(a), an obvious bonding interface hard to be obtained in dissimilar joints of heat-resistant steel to stainless steel [10,12,18,25,30] was observed between 316L and T91 steels. The interface originated from the top surface of the 316L side and gradually extended to the T91 side with the distance increasing from the weld surface. Then, the interface evolved to the 316L side again and ended near the weld center. In general, the weld root was the location where the bonding defect was preferentially developed due to insufficient material flow under the stir pin [26]. Hence, the bonding interface adjacent to the weld root was especially concerned here whereas no crack or void defect was found throughout the root region (Fig. 2(b)), indicating an excellent weld formation of dissimilar T91 steel to 316L steel.

At the T91 steel side, three microstructure regions of SZ, HAZ, and PM were found as shown in Fig. 2(c) (hereinafter referred to as T91-SZ, T91-HAZ, and T91-PM respectively,

316L steel side in kind). The HAZ could be divided into two subregions intituled HAZ1 and HAZ2 which exhibited disparate microstructural characteristics in the following section. At the 316L steel side, the joint could be divided into SZ, thermo-mechanically affected zone (TMAZ), and PM region (Fig. 2(d)), while the HAZ was not observed as shown in Fig. 2(e). As shown in Fig. 2(f), a mixing zone that 316L steel was involved in was found at the bottom of T91-SZ. This signified apparent material flow and strong mechanical mixing of the two as-welded materials.

3.2. Microstructure

3.2.1. T91 steel side

The typical microstructures of the T91-PM and T91-SZ were displayed in Fig. 3. As shown in Fig. 3(a)–(c), the T91-PM possessed a coarse martensite structure with a prior austenite grain size of ~20 μm. Precipitated phases could be found along the prior austenite grain boundaries (PAGBs) and inside the martensite due to the tempering heat-treatment process. As depicted by Zhang *et al.* [28] and He *et al.* [25], three kinds of precipitations including $M_{23}C_6$, M_3C, and MX were commonly generated in heat-resistant steels. Wherein, the globular $M_{23}C_6$ carbides were normally distributed along boundaries of prior austenite grains and martensite laths, while small globular MX carbonitride and needle-like M_3C carbides precipitated only in the martensite laths. According to the morphology features of the three precipitations, $M_{23}C_6$ and MX phases were clearly observed whereas the M_3C carbide was not found in the T91-PM (Fig. 4(a) and (b)). This was attributed to the metastable state of M_3C which could easily transform into $M_{23}C_6$ under tempering heat treatment [28]. Compared to the PM, an obvious microstructural refinement was detected in the SZ (Fig. 3(d)) where a martensitic structure with a high density of MX precipitations was generated (Figs. 3(e), 4(c), and 4(d)). Compared to the previous reports [18,25], more effective grain refinement was achieved in the T91-SZ with a prior austenite grain size of ~5 μm which was nearly a quarter of that of the PM (Fig. 3(f)).

The variation profiles of phase composition versus temperature were calculated by Thermo-Calc software as shown in Fig. 5. The phase transformation temperatures A_{c1} and A_{c3} were calculated as 820°C and 860°C for the T91 steel, respectively. Under the heat effects induced by friction and plastic deformation, the temperature of the SZ rapidly increased and reached a peak value beyond the A_{c3}. During this process, the martensite (α-Fe) in the SZ was transformed into austenite (γ-Fe) and the dissolution of precipitations occurred. In the single-phase austenite region, severe plastic deformation and dynamic recrystallization occurred under the rotational tool, and hence produced refined austenite which was transformed into martensite after the subsequent air cooling [31]. Generally, grain coarsening would proceed due to the high-temperature duration after the stirring process, and thus counteracted the structural refinement effect during the dynamic recrystallization process of FSW.

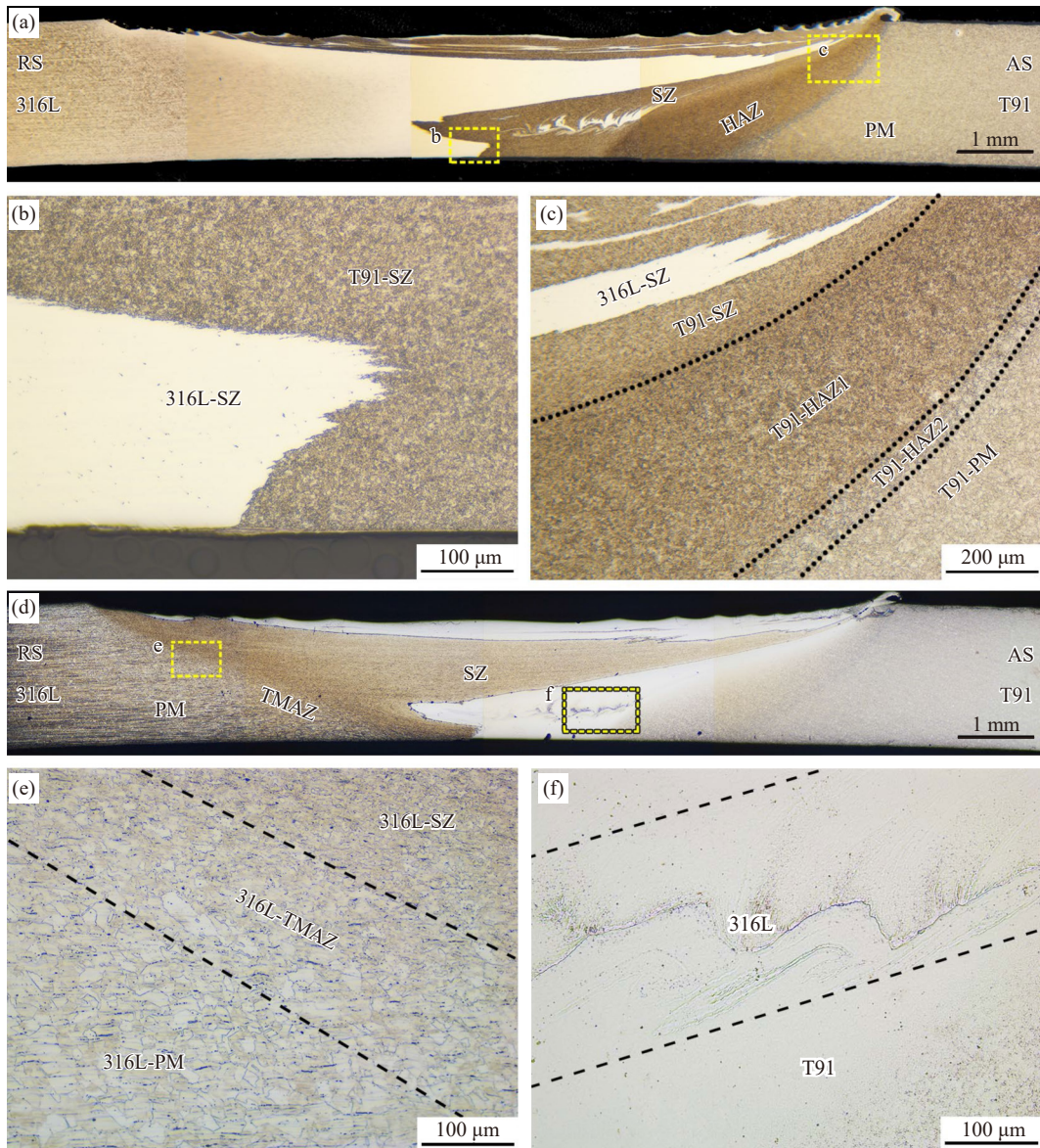In this work, the peak temperature and cooling rate were

Fig. 2. Cross-sectional OM morphologies etched by CuSO$_4$ solution (a–c) and oxalic acid solution (d–f) for displaying the macro-structures of T91 steel side and 316L steel side, respectively.
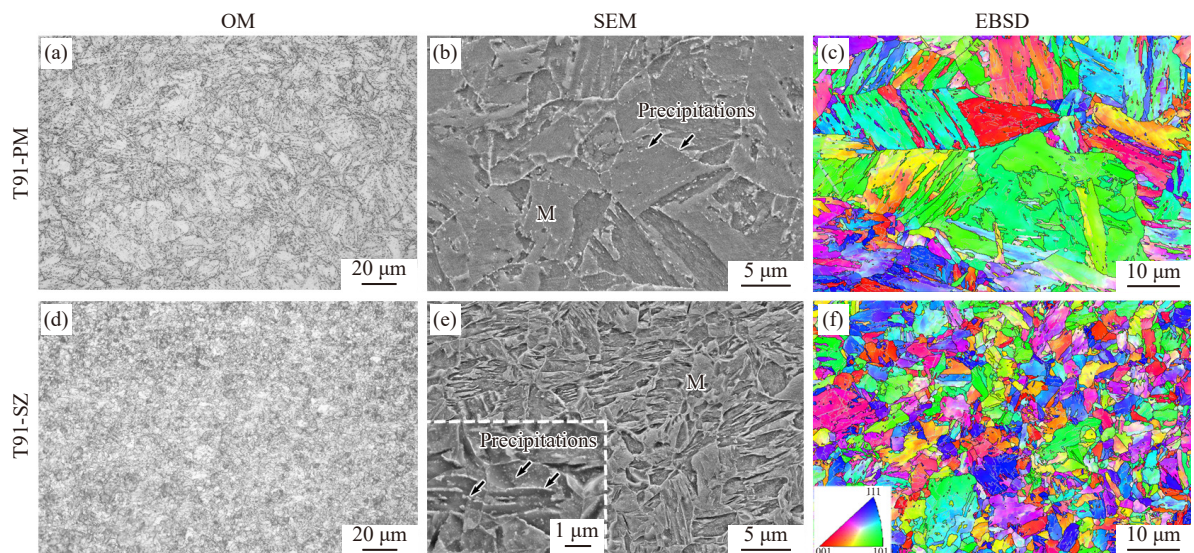

Fig. 3. Microstructures of T91 steel before and after FSW: (a–c) PM; (d–f) SZ. The insert in (e) indicates the enlarged SEM figure.
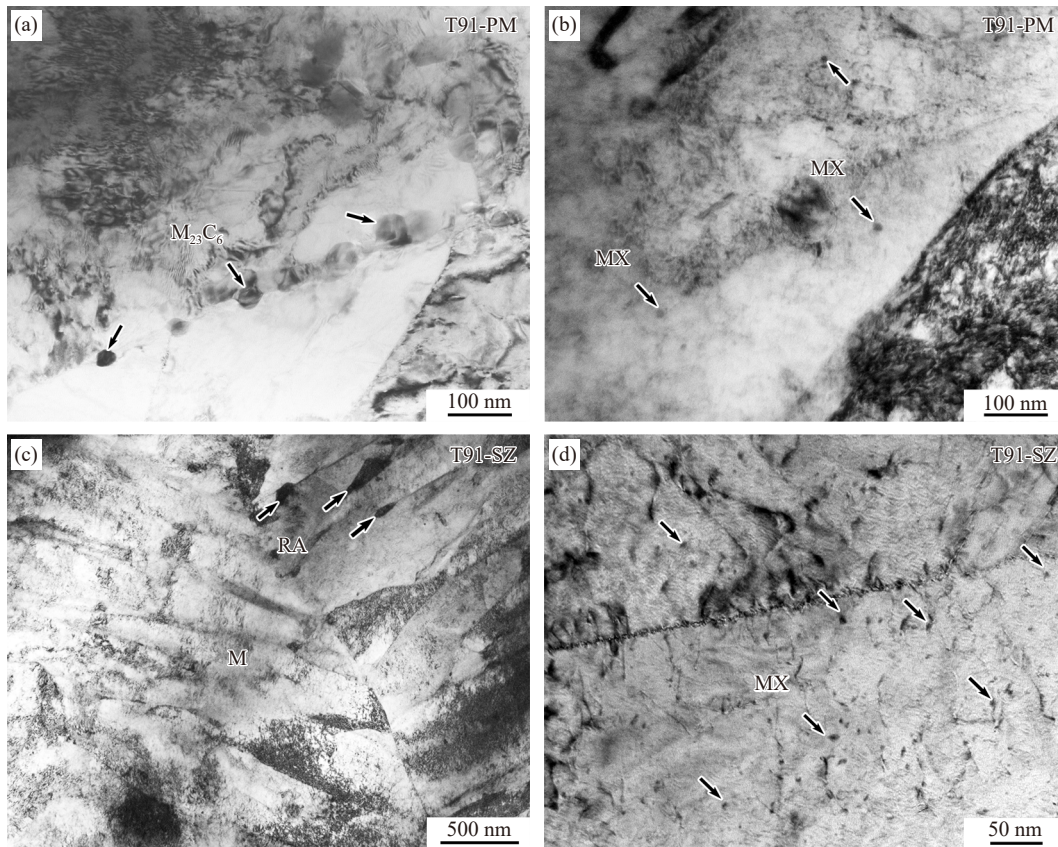
Fig. 4.   TEM images displaying the features of precipitations in the PM (a, b) and SZ (c, d) of T91 steel.
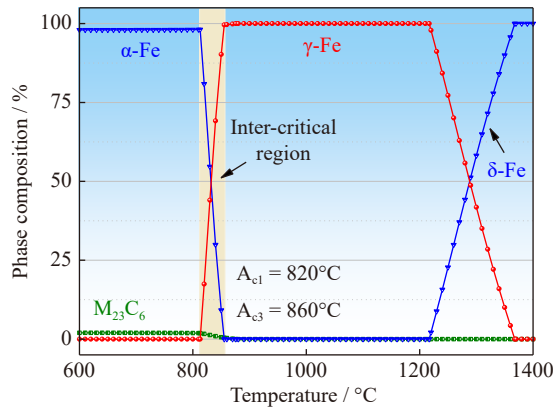

Fig. 5.   Composition evolution of equilibrium phase of T91 steel with temperature.

deliberately controlled by using a small-sized stir tool as well as a high welding speed, which enabled a relatively low peak temperature and a shortened duration time at the austenitic phase region. Therefore, the coarsening of austenite grains was suppressed and more effective refinement of martensite structure was achieved. Under the action of the welding heat cycle, the $M_{23}C_6$ carbides were dissolved into austenite and hard to be reprecipitated at room temperature due to rapid cooling. However, a large number of MX phases were formed due to the self-tempering effect of martensite which was usually observed during the quenching process of low carbide steels [32–34]. Owing to the rapid cooling, a small amount of retained austenite (RA) with a dark and vimineous appearance could be found near the martensitic lath boundar-

ies as revealed in Fig. 4(c).

In the HAZ1, three sites were chosen to disclose the structure changes as shown in Fig. 6(a). At the location near the SZ (site b), a martensite structure which was similar to that in the SZ was observed (Fig. 6(b1)). MX precipitations could be easily found in the martensite laths yet rarely discovered at the PAGBs (Fig. 6(b2)). At the location far from the SZ (site c), martensite with a structure size as large as that of the site a was observed (Fig. 6(c1)). Meanwhile, some $M_{23}C_6$ carbide particles were found inside the martensite (Fig. 6(c2)). At the location near the PM (site d), more $M_{23}C_6$ carbide particles together with some ferrite were observed in the martensite matrix (Fig. 6(d1) and (d2)). The formation of ferrite indicated that the peak temperature in this region was near A_{c3}.

From the above results, it could be validated that the microstructure in HAZ1 was not coarsened but refined compared to that in the SZ and PM. Some previous works ascribed this phenomenon to the recrystallization process that occurred in this region under the peak temperatures of near A_{c3} [25–26]. The rapid cooling in HAZ restrained the grain growth and promoted the formation of the refined martensitic structure [28]. In this work, we further improved the grain refinement of the HAZ1 by decreasing the peak temperature and increasing the cooling rate via the small stir tool and high welding speed. In addition, the $M_{23}C_6$ carbides were gradually dissolved with temperature increasing as shown in Fig. 5, which was the reason that $M_{23}C_6$ carbide was hard to be found at the location close to the SZ (site a).
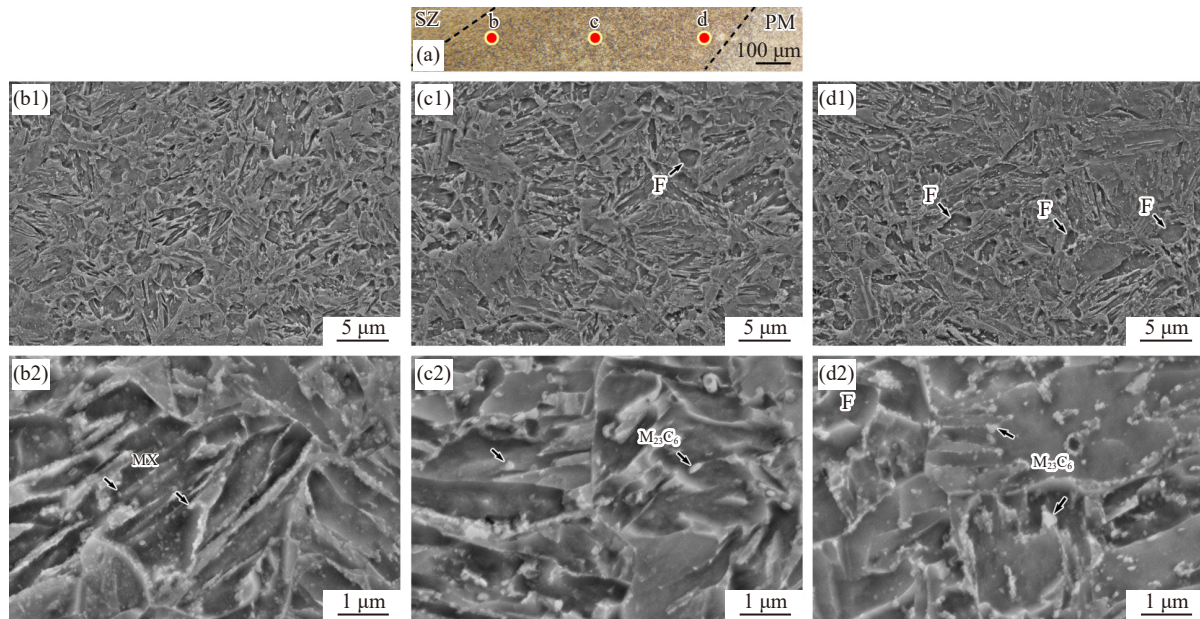
In the HAZ2, a ferrite/martensite dual-phase (DP) struc-

Fig. 6. Typical microstructures at different locations in T91-HAZ1: (a) OM morphology; (b1–d2) SEM images captured at the corresponding sites of b, c, and d in (a).

ture was generated as shown in Fig. 7. The HAZ2 was located between the HAZ1 and PM and suffered inferior peak temperature which was lower than that of the HAZ1 (Fig. 7(a) and (b)). The peak temperature in HAZ2 was between A_{c3} and A_{c1} which was marked as an inter-critical region as shown in Fig. 5. During the welding process, ferrite → austenite → martensite phase transformation proceeded in the HAZ2. However, a part of ferrite was not transformed into austenite and retained at the ambient temperature. Thus, partial austenitization was accomplished and the DP structure was obtained (Fig. 7(c)). In the DP structure, MX and $M_{23}C_6$ particles were clearly observed due to the self-tempering effect of martensite and the incomplete dissolution of $M_{23}C_6$ particles under the peak temperature between the inter-critical region. In addition, it should be noted that the HAZ2 owned a small width of less than 0.2 mm which was hard to be achieved in the previous studies [26,28].

3.2.2. 316L steel side

The microstructures in the 316L-SZ were observed as well

and obvious grain refinement was detected as shown in Fig. 8(a) and (d). The 316L-PM consisted of single-phase austenite with an average grain size of 13 μm (Fig. 8(b) and (c)). However, after severe plastic deformation and dynamic recrystallization, the coarse PM was refined to a uniform equiaxed structure with an average austenite grain size of 2.3 μm which was only one-sixth of that of the PM (Fig. 8(f)). This strong grain refinement was not achieved in the previous dissimilar FSW joints due to grain growth at elevated temperatures under high heat input conditions [18,25,35]. In addition, Cr-enriched phases which could deteriorate the corrosion resistance of SZ and HAZ were commonly found in FSW stainless steel joints [18,36], such as δ ferrite and σ phase [37–38]. However, by decreasing the peak temperature and enhancing the cooling rate, the development of δ ferrite and σ phase was suppressed because no obvious variation of phase composition was detected in the SZ and TMAZ compared with the PM (Figs. 8(e) and 9(b)). As shown in Fig. 9(a), material flow with an obvious shearing
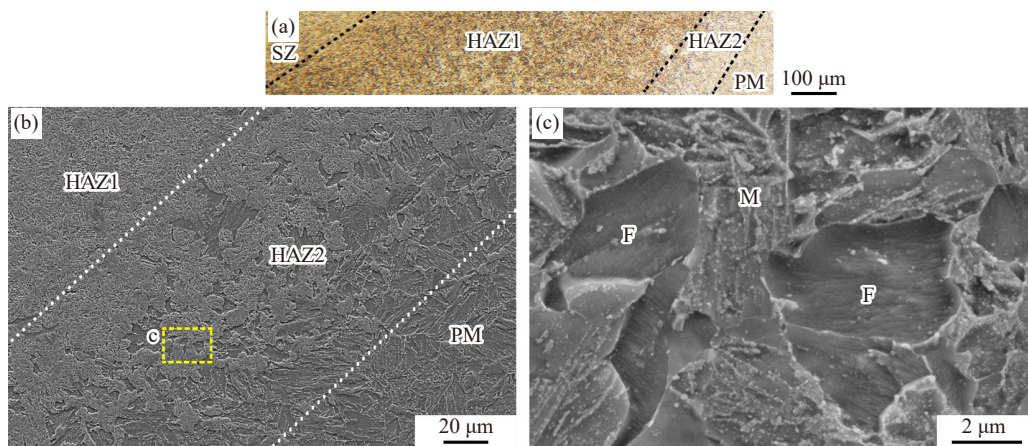

Fig. 7. Typical microstructures in T91-HAZ2: (a, b) overviews by OM and SEM respectively; (c) enlarged image of the marked region in (b).

OM   SEM   EBSD
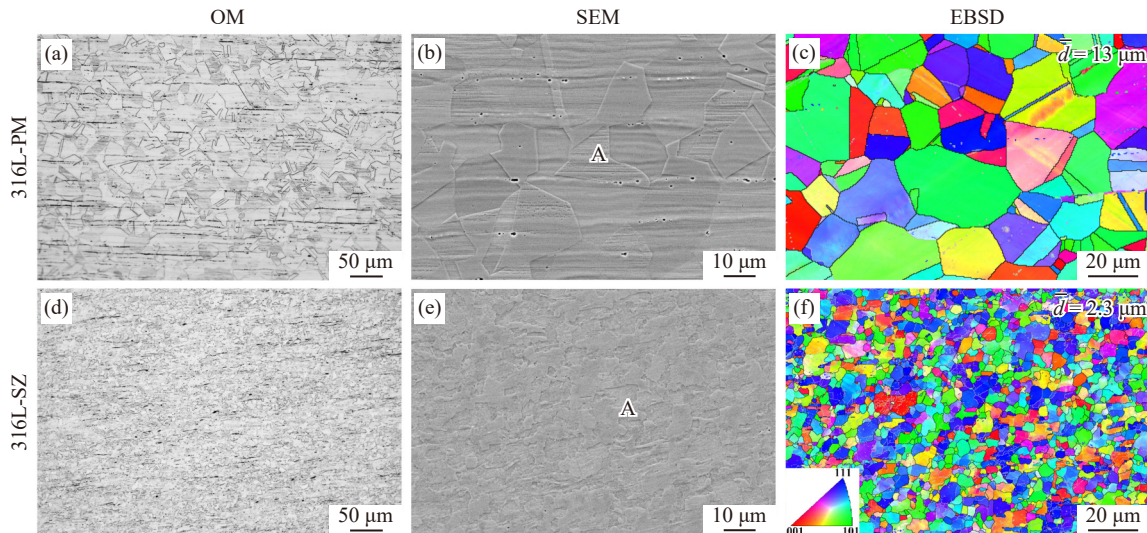

Fig. 8.   Microstructures of 316L steel before and after FSW: (a–c) PM; (d–f) SZ.
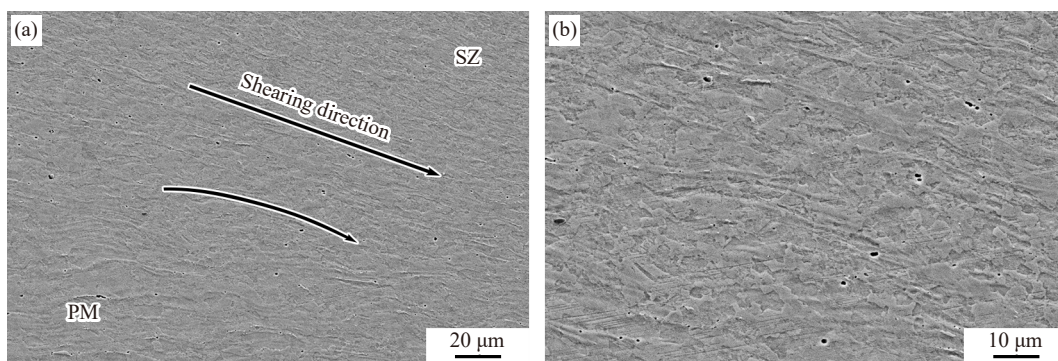

Fig. 9.   Material flow observed near TMAZ at 316L steel side: (a) low magnification image; (b) high magnification image.

direction from PM to SZ was detected, indicating a strong shear deformation of the grain structure in the TMAZ. However, the TMAZ was not found at the T91 side since the shearing morphology of austenite grain was covered up by the martensitic transformation. Similar phenomena were found in the FSW joints of DP [34] or Q&P steels [39].

3.2.3. Interface zone

The bonding interface played a crucial role in welded joints of dissimilar materials. A defect-free bonding interface with strong mechanical mixing and metallurgical bonding indicated excellent bonding strength of the two materials for welding. Fig. 10(a) shows the sound bonding interface obtained in the current work. An indented interface morphology was found between T91-SZ and 316L-SZ as shown in the enlarged image of Fig. 10(b). It is denoted that mechanical mixing was achieved between T91 and 316L steels as a result of the formation of a mixing zone in which the interface was involved. In order to reveal if there was element diffusion between these two steels, an EDS line scan was adopted across the interface. As shown in Fig. 10(c), gradient distributions of the main elements of Fe, Cr, and Ni were identified in the mixing zone, where an increase in Fe and decreases in Cr and Ni were found from the 316L steel side to the T91 steel side. Therefore, metallurgical bonding of 316L and T91 steels was successfully achieved. As shown in Fig. 11, the metallurgy feature of the interface was further in-

vestigated by TEM before which the foil specimen was accurately extracted via FIB (Fig. 11(a)). As shown in Fig. 11(b)–(d), a clear interface that possessed inhomogeneous composition of Ni element was found, while no apparent gradient distributions of Fe, Cr, and Mn were observed across the interface. This further confirmed the adequate element diffusion and metallurgical bonding of the interface on a micro-scale.

Fig. 10(d) is the EBSD image quality (IQ) map measured near the mixing zone. It is displayed that heterogeneous microstructures were obtained in the mixing zone. In the inverse pole figure (IPF) map of Fig. 10(e), it was evident that a fine grain subregion was formed in the mixing zone, where an obvious difference in the grain sizes could be detected compared to the adjacent regions of both the 316L and the T91 steels. As shown in Fig. 10(f), the fine grain subregion was located at the T91 side with a bcc crystal structure and abutted against the T91-SZ. Due to the considerable difference in the mechanical and thermal properties of 316L steel and T91 steel [2], mechanical incompatibility certainly existed in the mixing zone during the plastic deformation process of FSW. As shown in Table 1, the T91 steel had lower contents of Cr, Ni, Mo, and Mn elements compared to that of 316L steel. The element distinction signified a lower deformation resistance of the prior austenite of T91 steel due to the inferior strength at an elevated temperature arising from the
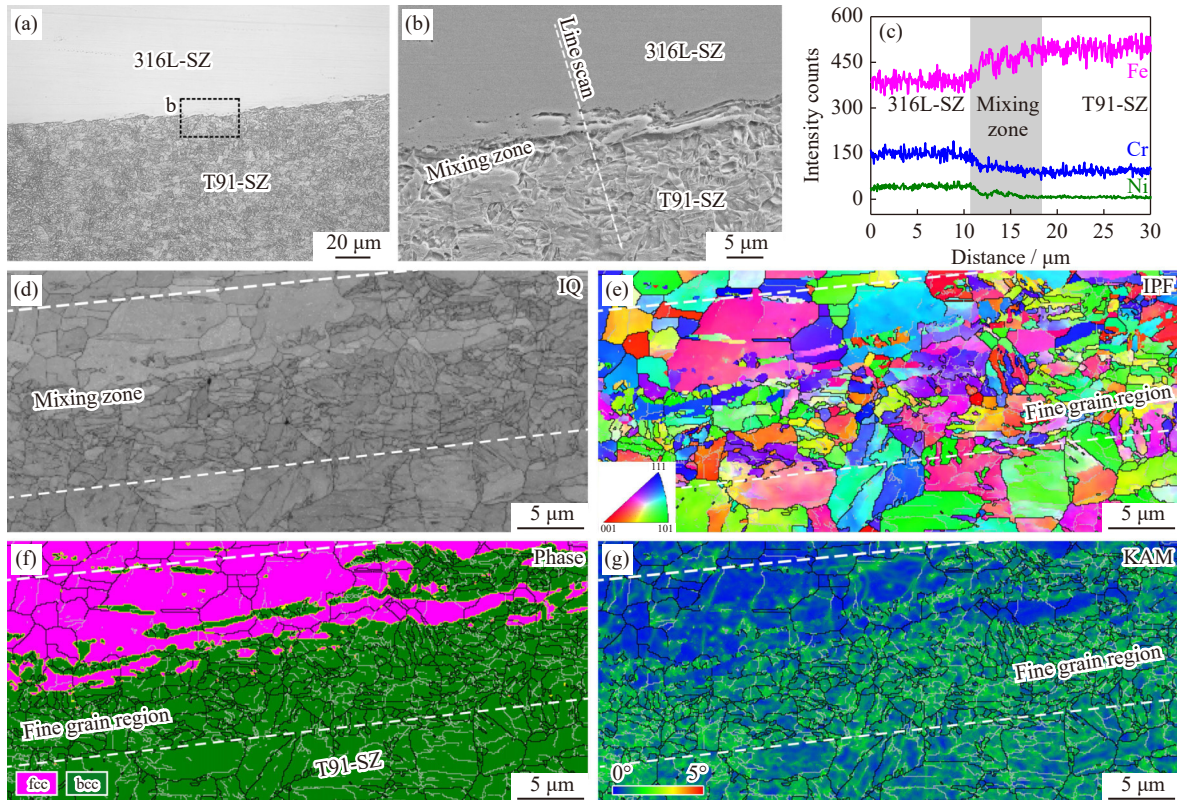
Fig. 10. Microstructural development adjacent to the bonding interface of dissimilar FSW joint: (a) OM image; (b) SEM image of the area b in (a); (c) EDS line scan results showing the element distributions across the interface (scan line as shown in (b)); (d-g) EBSD results exhibiting the grains (e), phases (f), and local misorientation (g).

lower content of solution elements. More severe plastic deformation might occur in the softer zone near the T91 side as verified by the high kernel average misorientation (KAM) in Fig. 10(g). Consequently, a subregion with smaller grain sizes was generated in the mixing zone near the T91 steel.

3.3. Mechanical properties

Fig. 12 shows the evolution of microhardness across the dissimilar FSW joint along with various directions. A valley-type hardness distribution with large value differences was observed in the normal direction (Fig. 12(a)). At the T91-SZ, the hardness was as high as HV 400, while low hardness values of nearly HV 200 were measured in the 316L-SZ. In the transverse direction, a great hardness increase was detected when the measuring point was located in the T91-SZ (Fig. 12(b)). The average hardness values of the 316L-PM steel and T91-PM were HV 149 and HV 276, respectively. However, the hardness values were increased by HV 50 and HV 130 in the SZs compared to the PMs of 316L steel and T91 steel, respectively. At T91-SZ, the refinement of the martensite structure was an important reason for the hardness enhancement due to grain refinement strengthening (Fig. 3). Besides, we concluded here that the precipitation hardening also played a crucial role in the hardness improvement. As revealed in Fig. 3(e) and Fig. 4(d), the high density of nano-sized MX phases could further strengthen the martensite by pining the mobile dislocations inner the martensite laths and astricting the plastic deformation of the martensite structure. As proposed above, the grain refine-

ment-induced hardening was the only mechanism for the hardness improvement in 316L-SZ, which was one of the reasons for the great microhardness distinction between T91-SZ and 316L-SZ.

HAZ was commonly a weak region in most of the steel joints, where premature failure occurred during tensile deformation due to material softening [39–40]. In the previous work [26], severe material softening with apparent hardness drop could be observed in the HAZ of heat-resistant steel, while the corresponding reason was not clarified. Here we achieved a dissimilar joint of T91 steel to 316L steel without obvious material softening for both the two steels. The hardness gradually decreased with the distance increasing from the SZ. In T91-HAZ, negligible material softening with a minor hardness decline compared to the PM was observed as shown in Fig. 12(b). The formation of the ferrite phase was the main reason for the material softening in this region (Fig. 7(b)), and a similar result was reported in the FSW research on martensitic steel [39]. The minimum hardness was confirmed to be located in the HAZ2 with decreasing amplitude of only HV ~10 compared to the hardness of adjacent PM (Fig. 13). In addition, the width of the softened zone was only ~0.1 mm, which was consistent with the narrow temperature range of only 40°C obtained in the inter-critical region (Fig. 5). Therefore, the softening degree and width of the softened zone were well controlled in the current FSW joint via the adjustment strategies of low peak temperature as well as high cooling rate. In order to ameliorate the heterogeneous microstructures and hardness across the as-welded joint,
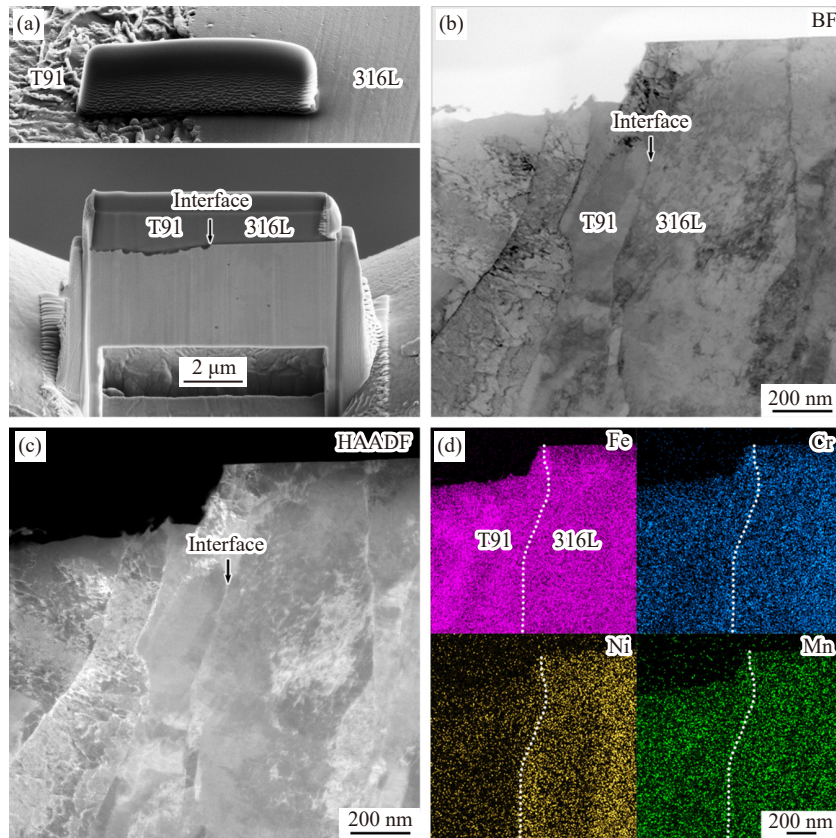
Fig. 11.   TEM results of the bonding interface: (a) sampling process via FIB; (b) bright field (BF) image; (c) high-angle annular dark field (HAADF) image; (d) EDS mapping results.
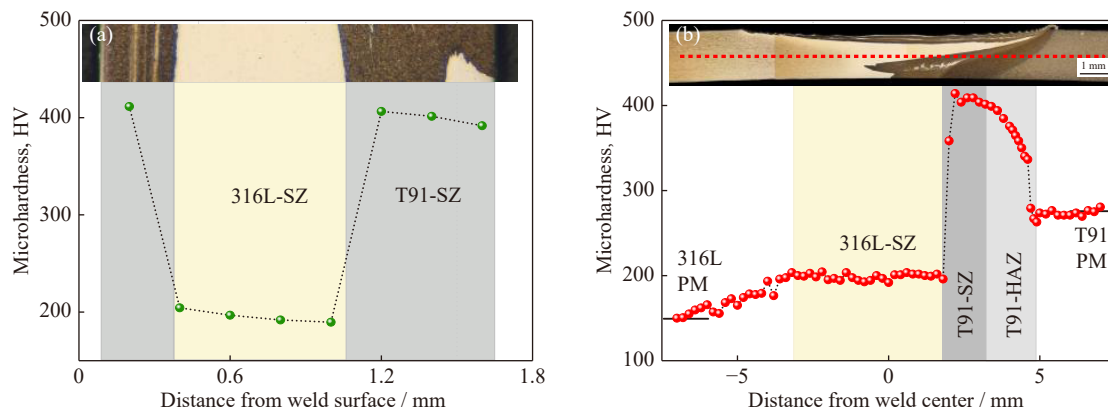

Fig. 12.   Microhardness distributions of dissimilar FSW joint along with the normal direction (a) and transverse direction (b).
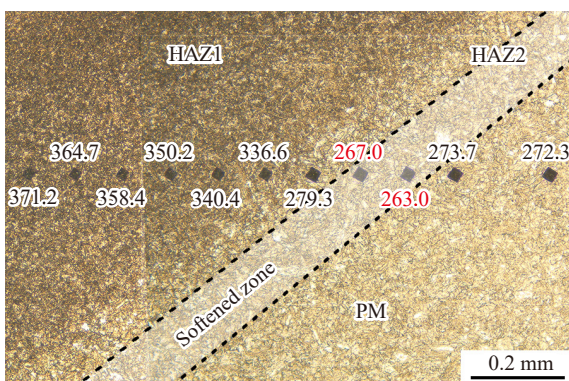

Fig. 13.   Microhardness values of T91 softened zone.

post-weld heat treatment has been proposed in an ongoing study which would be published in our future work.

The uniaxial tensile properties of the FSW joint and both PMs were exhibited in Fig. 14. As shown in the engineering stress–strain curves of Fig. 14(a), the 316L-PM owned a low yield strength (YS) of 307 MPa, an ultimate strength (UTS) of 627 MPa, and an excellent total elongation (TEL) of ~60%. The T91-PM possessed higher strength of both the YS and UTS, but the ductility was drastically lower than that of the 316L-PM. The YS, UTS, and TEL of 388 MPa, 640 MPa, and 17% were achieved respectively for the FSW joint. The YS of the FSW joint was increased by ~80 MPa (26%

increase) compared to that of the 316L-PM. In addition, the UTS of the joint was as high as that of the 316L-PM, demonstrating a high-strength dissimilar joint was fabricated in the present work. After the tensile test, the joint was broken in the PM region of the 316L side, as shown in the insert of Fig. 14(a). The fracture surface of the joint was full of dimples, voids, and tearing ridges and similar to that of the 316L-PM, indicating a good ductility of the joint (Fig. 14(b)).

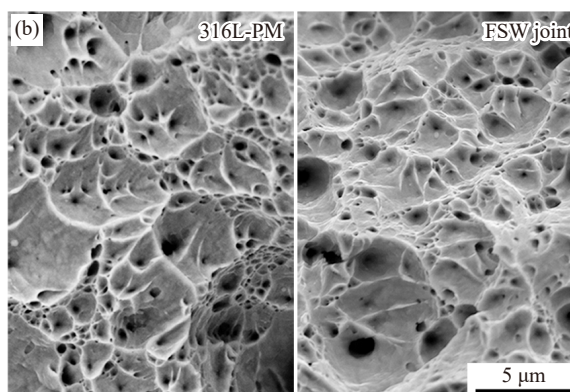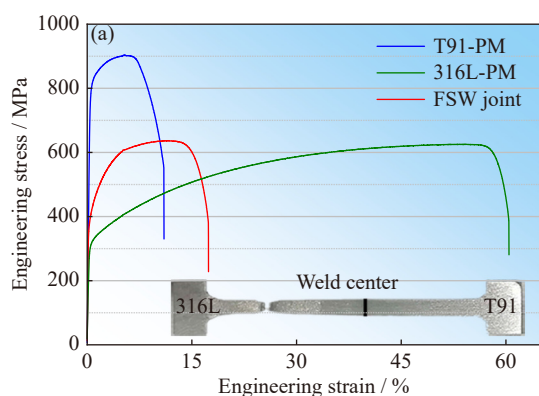From the above discussions, it was inferred that the excellent tensile strength of the FSW joint was closely related to the microstructural modification achieved in both the as-welded steels. The dependable bonding interface as well as the hardening of the dissimilar joint without apparent material softening avoided the severe deformation and failure in the weld zone, and hence transformed the plastic strain to the soft material of 316L-PM where eventual fracture developed. Therefore, the high-strength dissimilar joint of T91 steel to 316L steel was achieved via the FSW technique which could apply to other steel materials for producing high-quality dissimilar weldments.

Fig. 14. Tensile testing results of the FSW joint and PMs: (a) engineering stress–strain curves; (b) fracture morphologies of 316L-PM and FSW joint. The insert in (a) shows the failure location of the joint.

4. Conclusions

In this work, the high-strength dissimilar joint of T91 heat-resistant steel to 316L stainless steel was successfully fabricated via the FSW technique. The main conclusions are as follows.

(1) Defect-free joint with a large bonding interface could be produced using a small-sized tool with a rotational rate of 400 r/min as well as a relatively higher welding speed of 150 mm/min. When the higher or lower rotational rate of 500 or 300 r/min was adopted, crack or tunnel defect would generate respectively due to the inappropriate material flow.

(2) Typical SZ and PM regions were found at both the T91 steel side and the 316L steel side. However, the HAZ (including two subregions) was only observed at the T91 steel side and the TMAZ was only visible at the 316L steel side. Unprecedented grain refinement was achieved in both the T91-SZ and the 316L-SZ. The microstructure in T91-HAZ1 was not coarsened but refined compared to that of the T91-PM. The ferrite/martensite DP structure was found in the T91-HAZ2.

(3) A strong bonding interface was formed via both the mechanical mixing and metallurgical bonding between these two as-welded steels. A mixing zone with heterogeneous microstructures and gradient distributions of Fe, Cr, and Ni elements was found around the interface. In the mixing zone, a fine grain subregion was developed at the T91 side due to the mechanical incompatibility of 316L steel and T91 steel.

(4) No obvious material softening was detected in the dissimilar joint except a negligible hardness decline of only HV ~10 in the T91-HAZ2 due to the formation of the ferrite phase. The FSW joint presented excellent UTS as high as that of the 316L-PM and a considerable improvement of the YS. Tensile failure in the 316L-PM was observed in the joint with a ductile fracture morphology on account of the dependable weld zone.

Acknowledgements

Conflict of Interest

The authors declare that they have no known conflict of interest.

References

[1] R. Viswanathan, J.F. Henry, J. Tanzosh, *et al*, U.S. program on materials technology for ultra-supercritical coal power plants, *J. Mater. Eng. Perform.*, 14(2005), No. 3, p. 281.

[2] S.J. Zinkle and G.S. Was, Materials challenges in nuclear energy, *Acta Mater.*, 61(2013), No. 3, p. 735.

[3] S.J. Zinkle and J.T. Busby, Structural materials for fission & fusion energy, *Mater. Today*, 12(2009), No. 11, p. 12.

[4] Y. Gong, Z.G. Yang, and F.Y. Yang, Heat strength evaluation and microstructures observation of the welded joints of one China-made T91 steel, *J. Mater. Eng. Perform.*, 21(2012), No.

7, p. 1313.

[5] M. Ida, T. Chida, K. Furuya, E. Wakai, H. Nakamura, and M. Sugimoto, Thermal-stress analysis of IFMIF target back-wall made of reduced-activation ferritic steel and austenitic stainless steel, *J. Nucl. Mater.*, 386-388(2009), p. 987.

[6] J.H. Zhou, Y.F. Shen, and N. Jia, Strengthening mechanisms of reduced activation ferritic/martensitic steels: A review, *Int. J. Miner. Metall. Mater.*, 28(2021), No. 3, p. 335.

[7] C. Li, X.D. Fang, Q.S. Wang, *et al*, A synergy of different corrosion failure modes pertaining to T91 steel impacted by extreme lead–bismuth eutectic flow pattern, *Corros. Sci.*, 180(2021), art. No. 109214.

[8] C. Li, Y.J. Liu, F.F. Zhang, X.D. Fang, and Z. Liu, Erosion-corrosion of 304N austenitic steels in liquid PbBi flow perpendicular to steel surface, *Mater. Charact.*, 175(2021), art. No. 111054.

[9] J.Y. Zhang, B. Huang, Q.S. Wu, C.J. Li, and Q.Y. Huang, Effect of post-weld heat treatment on the mechanical properties of CLAM/316L dissimilar joint, *Fusion Eng. Des.*, 100(2015), p. 334.

[10] R.S. Vidyarthy, A. Kulkarni, and D.K. Dwivedi, Study of microstructure and mechanical property relationships of A-TIG welded P91–316L dissimilar steel joint, *Mater. Sci. Eng. A*, 695(2017), p. 249.

[11] S.K. Albert, C.R. Das, S. Sam, *et al*, Mechanical properties of similar and dissimilar weldments of RAFMS and AISI 316L (N) SS prepared by electron beam welding process, *Fusion Eng. Des.*, 89(2014), No. 7-8, p. 1605.

[12] I. Serre and J.B. Vogt, Mechanical properties of a 316L/T91 weld joint tested in lead-bismuth liquid, *Mater. Des.*, 30(2009), No. 9, p. 3776.

[13] J. van den Bosch and A. Almazouzi, Compatibility of martensitic/austenitic steel welds with liquid lead bismuth eutectic environment, *J. Nucl. Mater.*, 385(2009), No. 3, p. 504.

[14] H.Y. Fu, T. Nagasaka, M. Yamazaki, *et al*, Deformation of dissimilar-metals joint between F82H and 316L in impact tests after neutron irradiation, *Fusion Eng. Des.*, 124(2017), p. 1063.

[15] H. Serizawa, D. Mori, Y. Shirai, H. Ogiwara, and H. Mori, Weldability of dissimilar joint between F82H and SUS316L under fiber laser welding, *Fusion Eng. Des.*, 88(2013), No. 9-10, p. 2466.

[16] H. Serizawa, D. Mori, H. Ogiwara, and H. Mori, Effect of laser beam position on mechanical properties of F82H/SUS316L butt-joint welded by fiber laser, *Fusion Eng. Des.*, 89(2014), No. 7-8, p. 1764.

[17] Y. Li, Y.P. Zeng, and Z.C. Wang, Interfacial microstructure evolution of 12Cr1MoV/TP347H dissimilar steel welded joints during aging, *Int. J. Miner. Metall. Mater.*, 28(2021), No. 9, p. 1497.

[18] D. Sunilkumar, S. Muthukumaran, M. Vasudevan, and M.G. Reddy, Effect of friction stir and activated-GTA welding processes on the 9Cr–1Mo steel to 316LN stainless steel dissimilar weld joints, *Sci. Technol. Weld. Join.*, 25(2020), No. 4, p. 311.

[19] R.S. Mishra and Z.Y. Ma, Friction stir welding and processing, *Mater. Sci. Eng. R*, 50(2005), No. 1-2, p. 1.

[20] Z.Y. Ma, A.H. Feng, D.L. Chen, and J. Shen, Recent advances in friction stir welding/processing of aluminum alloys: Microstructural evolution and mechanical properties, *Crit. Rev. Solid State Mater. Sci.*, 43(2018), No. 4, p. 269.

[21] Q. Shang, D.R. Ni, P. Xue, B.L. Xiao, and Z.Y. Ma, Improving joint performance of friction stir welded wrought Mg alloy by controlling non-uniform deformation behavior, *Mater. Sci. Eng. A*, 707(2017), p. 426.

[22] S.C. Han, L.H. Wu, C.Y. Jiang, *et al*, Achieving a strong polypropylene/aluminum alloy friction spot joint *via* a surface laser processing pretreatment, *J. Mater. Sci. Technol.*, 50(2020),

p. 103.

[23] F.C. Liu, Y. Hovanski, M.P. Miles, C.D. Sorensen, and T.W. Nelson, A review of friction stir welding of steels: Tool, material flow, microstructure, and properties, *J. Mater. Sci. Technol.*, 34(2018), No. 1, p. 39.

[24] D.G. Mohan and C.S. Wu, A review on friction stir welding of steels, *Chin. J. Mech. Eng.*, 34(2021), art. No. 137.

[25] B. He, L. Cui, D.P. Wang, Y.C. Liu, C.X. Liu, and H.J. Li, The metallurgical bonding and high temperature tensile behaviors of 9Cr–1W steel and 316L steel dissimilar joint by friction stir welding, *J. Manuf. Process.*, 44(2019), p. 241.

[26] B. He, L. Cui, D.P. Wang, H.J. Li, and C.X. Liu, Microstructure and mechanical properties of RAFM–316L dissimilar joints by friction stir welding with different butt joining modes, *Acta Metall. Sin. Engl. Lett.*, 33(2020), No. 1, p. 135.

[27] W.S. Tang, X.Q. Yang, S.L. Li, and H.J. Li, Microstructure and properties of CLAM/316L steel friction stir welded joints, *J. Mater. Process. Technol.*, 271(2019), p. 189.

[28] C. Zhang, L. Cui, D.P. Wang, Y.C. Liu, C.X. Liu, and H.J. Li, The heterogeneous microstructure of heat affect zone and its effect on creep resistance for friction stir joints on 9Cr–1.5W heat resistant steel, *Scripta. Mater.*, 158(2019), p. 6.

[29] M. Türkan and Ö. Karakaş, Numerical modeling of defect formation in friction stir welding, *Mater. Today Commun.*, 31(2022), art. No. 103539.

[30] F.J. Martín-Muñoz, L. Soler-Crespo, and D. Gómez-Briceño, Assessment of the influence of surface finishing and weld joints on the corrosion/oxidation behaviour of stainless steels in lead bismuth eutectic, *J. Nucl. Mater.*, 416(2011), No. 1-2, p. 80.

[31] Z.W. Wang, M. Liu, H. Zhang, *et al*, Welding behavior of an ultrahigh-strength quenching and partitioning steel by fusion and solid-state welding methods, *J. Mater. Res. Technol.*, 17(2022), p. 1289.

[32] Z.W. Wang, G.N. Ma, B.H. Yu, *et al*, Improving mechanical properties of friction-stir-spot-welded advanced ultra-high-strength steel with additional water cooling, *Sci. Technol. Weld. Joining*, 25(2020), No. 4, p. 336.

[33] S. Sackl, H. Clemens, and S. Primig, Investigation of the self tempering effect of martensite by means of atom probe tomography, *Pract. Metallogr.*, 52(2015), No. 7, p. 374.

[34] Z.W. Wang, G.M. Xie, D. Wang, *et al*, Microstructural evolution and mechanical behavior of friction-stir-welded DP1180 advanced ultrahigh strength steel, *Acta Metall. Sin. Engl. Lett.*, 33(2020), No. 1, p. 58.

[35] M. Shamanian, A. Mirzaei, J. Kangazian, and J.A. Szpunar, Characterization and mechanical behavior of AISI 316L/Incoloy 825 dissimilar welds processed by friction stir welding, *J. Manuf. Process.*, 55(2020), p. 66.

[36] Y.C. Chen, H. Fujii, T. Tsumura, *et al*, Friction stir processing of 316L stainless steel plate, *Sci. Technol. Weld. Joining*, 14(2009), No. 3, p. 197.

[37] S.H.C. Park, Y.S. Sato, H. Kokawa, K. Okamoto, S. Hirano, and M. Inagaki, Rapid formation of the sigma phase in 304 stainless steel during friction stir welding, *Scripta. Mater.*, 49(2003), No. 12, p. 1175.

[38] S.H.C. Park, Y.S. Sato, H. Kokawa, K. Okamoto, S. Hirano, and M. Inagaki, Corrosion resistance of friction stir welded 304 stainless steel, *Scripta Mater.*, 51(2004), No. 2, p. 101.

[39] Z.W. Wang, J.F. Zhang, G.M. Xie, *et al*, Evolution mechanisms of microstructure and mechanical properties in a friction stir welded ultrahigh-strength quenching and partitioning steel, *J. Mater. Sci. Technol.*, 102(2022), p. 213.

[40] P.C. Zhu, L. Zhang, Z.C. Li, *et al*, Microstructure and mechanical properties of friction stir welded 1.5 GPa martensitic high-strength steel plates, *Acta Metall. Sin. Engl. Lett.*, 35(2022), No. 7, p. 1079.